Diammonium-Mediated Perovskite Film Formation for High-Luminescence Red Perovskite Light-Emitting Diodes

Nan Li, Sofia Apergi, Christopher C. S. Chan, Yongheng Jia, Fangyan Xie, Qiong Liang, Gang Li, Kam Sing Wong, Geert Brocks, Shuxia Tao,* and Ni Zhao*

3D mixed-halide perovskite-based red emitters combine excellent charge-transport characteristics with simple solution processing and good film formation; however, light-emitting diodes (LEDs) based on these emitters cannot yet outperform their nanocrystal counterparts. Here the use of diammonium halides in regulating the formation of mixed bromide–iodide perovskite films is explored. It is found that the diammonium cations preferentially bond to Pb–Br, rather than Pb–I, octahedra, promoting the formation of quasi-2D phases. It is proposed that the perovskite formation is initially dominated by the crystallization of the thermodynamically more favorable 3D phase, but, as the solution gets depleted from the regular A cations, thin shells of amorphous quasi-2D perovskites form. This leads to crystalline perovskite grains with efficiently passivated surfaces and reduced lattice strain. As a result, the diammonium-treated perovskite LEDs demonstrate a record luminance (10745 cd m^{-2}) and half-lifetime among 3D perovskite-based red LEDs.

1. Introduction

Since the first demonstration of room-temperature electroluminescence devices based on metal halide perovskites in 2014,[1] the field of perovskite light-emitting diode (PeLED) has progressed rapidly, achieving devices with high external quantum efficiency (>20%), excellent color purity (with full width at half-maximum (FWHM) below 20 nm in the emission spectrum[2]) and wide color gamut. On the other hand, lattice instability and material degradation caused by heat and electric field during intensive current stressing remain detrimental for the performance of PeLEDs and hinder the commercialization of this technology.

Red-emitting PeLEDs are a critical component for both display and biomedical applications. One of the most popular strategies to combat instability in red perovskite emitters is dimension regulation. Highly efficient red PeLEDs have been fabricated by employing perovskite quantum dots (QDs) and multiple quantum well (MQW) perovskites to manipulate emission wavelength and confine excitons.[3–7] However, the hot-injection synthesis and post treatment of QDs require complex processing and high efficiencies can only be achieved at a low current density. The quantum-well width in MQW perovskites also needs to be finely regulated to avoid small-n phases and guarantee efficient energy transfer.[8,9] 3D perovskites converted directly from precursor mixtures would be more desirable because of simple fabrication and efficient charge transport. A mixture of bromide and iodide ions is generally required to construct 3D perovskite lattices that emit red light. In this case the formation of defects during the 3D film formation is almost inevitable. Various passivation strategies have been developed to address this issue and improved both the device efficiency by removing nonradiative

N. Li, Y. Jia, N. Zhao
Department of Electronic Engineering
The Chinese University of Hong Kong
New Territories, Hong Kong
E-mail: nzhao@ee.cuhk.edu.hk

S. Apergi, G. Brocks, S. Tao
Department of Applied Physics
Eindhoven University of Technology
Eindhoven 5600 MB, The Netherlands
E-mail: s.x.tao@tue.nl

C. C. S. Chan, K. S. Wong
Department of Physics
William Mong Institute of Nano Science and Technology
The Hong Kong University of Science and Technology
Clearwater Bay, Hong Kong

F. Xie
Instrumental Analysis and Research Center
Sun Yat-sen University
Guangzhou 510275, P. R. China

Q. Liang, G. Li
Department of Electronic and Information Engineering
The Hong Kong Polytechnic University
Kowloon, Hong Kong

G. Brocks
Faculty of Science and Technology
University of Twente
Enschede 7500AE, The Netherlands

The ORCID identification number(s) for the author(s) of this article can be found under https://doi.org/10.1002/adma.202202042.

recombination centers and operational stability by suppressing ion migration under continuous working conditions.[10–13] Yet, the overall performance of the 3D perovskite-based red PeLEDs still significantly lags behind that of QD- and MQW-based LEDs.

Organic ammonium halides are some of the most popular passivation agents for perovskites. An organic ammonium cation can occupy the A-site of a perovskite lattice, while leaving the halide ion to occupy the X-site and passivate the undercoordinated Pb^{2+} ion.[14] Ammonium halides such as imidazolium iodide,[10] 2-naphthylmethylammonium iodide,[15] and 4-fluorophenylmethylammonium iodide[16] have been demonstrated to passivate lead and halide defects in 3D perovskites-based PeLEDs and enhance the luminescence efficiency and long-term stability to a certain extent. Yet the performances of these modified devices are still significantly lower than those of the perovskite QD- and MQW-based LEDs, suggesting a more fundamental intervention of the passivation agent to the 3D perovskite formation is required. Apart from the monoammonium halides, diammonium molecules with two amino group tails are explored much less. Yet, they might potentially be even more successful in passivating defects and improving device stability due to the stronger binding of the diammonium cations with the perovskite lattice.[17] Previously, diammonium halides were mainly introduced to produce Dion–Jacobson (DJ) structured MQW perovskites, which altered phase formation to enhance the material stability.[18–20] The design also provides a material platform for tuning energy funneling, although precise control of the phase type and distribution remains a challenge. Despite these handful of demonstrations of diammonium halide additive-modified PeLEDs, it remains unclear whether diammonium cations can address the limitations of monoammonium cations in modulating the film formation process and electronic properties of the mixed halide 3D perovskite systems.

In this work, we present a new approach for fabricating efficient and stable red PeLEDs by passivating 3D perovskite emitters using a diammonium molecule, without creating MQW structures at the same time. Specifically, ethylenediammonium dibromide ($EDABr_2$) with a molar ratio of 20% is introduced in the perovskite precursor solution. The resulting films exhibit an island morphology with the diammonium molecule bonding to 3D grain surfaces that are Br-rich. Combining X-ray photoelectron spectroscopy (XPS) analysis with density functional theory (DFT) calculations, we propose a growth mechanism for the EDA-treated perovskite, where EDA-Br rich amorphous quasi-2D phases form as capping layers at the 3D perovskite grain surfaces, thus passivating defects, suppressing ion migration, and reducing lattice strain. As a result, the optimized device shows a peak external quantum efficiency (EQE) of 17.03% at 671 nm and a record luminance of 10 745 cd m^{-2} with FWHM of 28 nm. An operational half-lifetime of 15.4 h has been obtained, which is the longest among the red-emissive 3D PeLEDs.

2. Results and Discussion

We fabricate cesium (Cs)-based lead mixed bromide/iodide perovskite thin films by a simple one-step solution process without any antisolvent washing or solvent vapor (such as

DMF vapor) post treatment. The $EDABr_2$ additive is introduced in the perovskite precursor solution with a molar ratio varied between 10% to 60%. (The fabrication details are described in the Experimental Section.) The control perovskite film (i.e., the perovskite film without $EDABr_2$) exhibits a continuous film morphology, while the films with 10% or 20% $EDABr_2$ additive turn into isolated grains of a few hundred nanometers in size (**Figure 1** and Figure S1, Supporting Information) following an apparently retarded crystallization process (Figures S2 and S3, Supporting Information; The film formation mechanism will be discussed in detail in later sections). The further increase in the $EDABr_2$ ratio leads to agglomeration of grains and reduction of crystallinity (Figure 1c). By comparing the optical and electronic properties of the modified perovskite films (data shown in the following sections), we have identified 20% as the optimal molar ratio for the $EDABr_2$ additive. The island-shaped morphology with decreased gain sizes could potentially improve the light outcoupling of the devices via enhanced light scattering by the discrete grains.[21–23] It is worth noting that no diffraction peaks corresponding to crystalline small-n 2D perovskite phases are detected in the X-ray diffraction (XRD) patterns of the modified films (Figure 1c), which is in accordance with the absence of the 2D excitonic peaks in the absorption spectra (Figure S4, Supporting Information). Also, the transient absorption (TA) spectra of the perovskite film exhibit little change after the $EDABr_2$ modification (Figure S5, Supporting Information). Thus, the addition of $EDABr_2$ does not seem to induce crystalline MQW perovskites.

To probe the interaction between the diammonium cations and the perovskite, we carry out XPS measurements. According to the significant increase of C and N signals at the surface in the XPS depth profiles of the modified film (Figure S6, Supporting Information), we conclude that EDA^{2+} cations are mainly distributed at grain boundaries and surfaces instead of being incorporated in the 3D bulk lattice. This means that after the annealing process, the films remain in a 3D bulk phase, instead of in a MQW phase for instance. In addition, the Br:Pb ratio at the surface of the modified film is higher than that in the bulk (Figure 1d). A larger difference between the surface Br:I ratio and bulk Br:I ratio is observed in the modified film compared with that in the control film (Figure 1e). Interestingly, the Br 3d signal of the modified perovskite is quite different from that of the control sample, with the former resembling more the signal of the $EDAPbBr_4$ perovskite instead of the $EDABr_2$ molecules (Figure 1f), suggesting that the surface Br ions in the modified film are most likely reside in a perovskite phase rather than free molecules.[24] However, this is not the case for I, where no obvious variation of its chemical environment is observed (Figure 1g). The increased difference between the surface and bulk Br:I ratios indicates that EDA^{2+} ions prefer to attract Br^- ions and bond with the $PbBr_6^{4-}$ octahedra, and not PbI_6^{4-} octahedra.

To help understanding the effect of the $EDABr_2$ additive on the formation of the perovskite, we calculate the formation energies of the 3D $CsPbX_3$ (X = Br, I) perovskites and several $EDACs_{n-1}Pb_nX_{3n+1}$ (n = 1–4) quasi-2D perovskites using DFT calculations (see atomistic structures and lattice parameters in Figure S7 and Table S1, Supporting Information). As shown in **Figure 2**a, Br-based perovskites have notably lower formation

**ADVANCED
SCIENCE NEWS**

www.advancedsciencenews.com

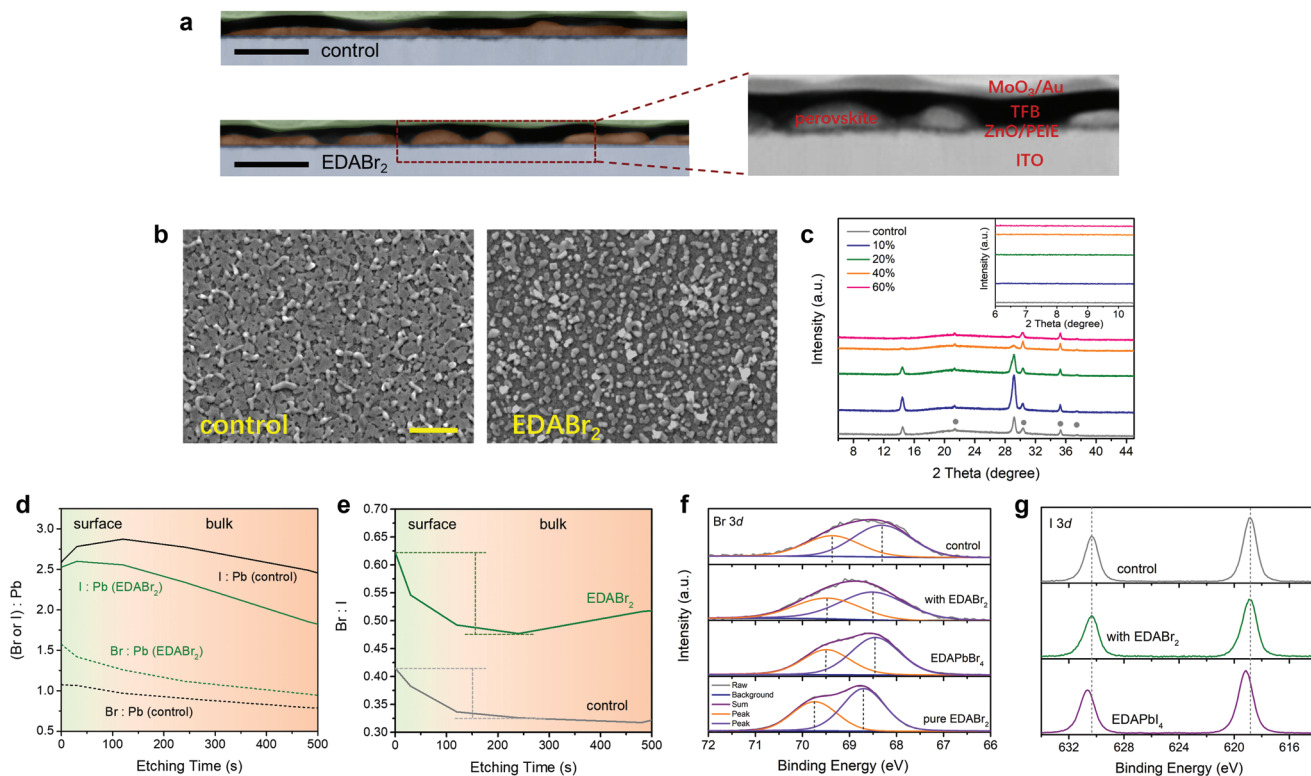**ADVANCED
MATERIALS**

www.advmat.de

Figure 1. Characterizations of perovskite films. a,b) Cross-sectional HAADF-STEM images (a) and top-view SEM images (b) of the control film and EDABr$_2$-modified films. The scale bars in (a) and (b) are 200 nm and 1 μm, respectively. c) XRD patterns of the fabricated films. d,e) XPS depth profiling of X:Pb ratio (d) and Br:I ratio (e) for the control perovskite (gray line) and modified perovskite (green line). f) Br 3d XPS spectra and g) I 3d XPS spectra for the fabricated films.

energies than I-based ones, the difference being more than 0.3 eV per PbI$_3$ unit for $n > 1$. In addition, the 3D perovskites show much lower formation energies than the EDACs$_{n-1}$Pb$_n$X$_{3n+1}$ phases with small n values. The formation energy of the latter phases becomes lower with increasing n, gradually approaching that of the 3D phase, as one might expect. For example, the difference in formation energy between the $n = 4$ phase and 3D phase is ≈0.05 eV for I perovskites and 0.1 eV for Br perovskites. These results suggest that if the concentration of EDA^{2+} in the mixed precursor is sufficiently high, some large-n Br-rich quasi-2D phases are quite likely to form.

It is worth noting that when n increases from 4 to ∞ (i.e., 3D phase), the formation energy of the EDA-based perovskites EDACs$_{n-1}$PbnX$_{3n+1}$ drops gradually in a narrow range (Figure 2a). Therefore, it is quite likely that the EDA-Br rich phase consists of mixed 2D layers with different n values, where clusters of diverse sizes (containing various numbers of PbBr$_6^{4-}$ octahedra) are assembled and interconnected by the EDA^{2+} ligands in a disordered fashion. Combining this theoretical insight with the TA, XPS and XRD results, we speculate that the EDA^{2+} ligands may promote the growth of mixed large-n phases at the atomistic scale, leading to an amorphous nature of the surface perovskite phase at the microscopic scale.

Based on the above experimental and theoretical observations, we propose the following model for the formation process of the modified perovskite film (Figure 2b). As the formation energies of the 3D perovskites are the lowest, during perovskite

formation reaction 3D phases will form first (Stage I). Towards the late stage of 3D perovskite formation, Cs$^+$ ions are depleted and the EDA^{2+}/Cs$^+$ ratio in the precursor becomes high. When that happens, the formation of EDA-containing phases occurs (Stage II). These phases will most probably be Br-rich due to the high formation energies of the I-rich phases. Finally, at Stage III, the perovskite films grow into uniform 3D mixed halide grains, surrounded by EDA-Br rich perovskite phases.

We next investigate the defect formation energies of Br vacancies at an EDA^{2+} and Br$^-$ ions dominated perovskite interface. We take the $n = 4$ perovskite, EDACs$_3$Pb$_4$Br$_{13}$, to represent the EDA-Br passivated perovskite, and compare the vacancy formation energies with those in CsPbBr$_3$ as the reference 3D perovskites. Our results (shown in Figure 2c) indicate that making a Br vacancy on a Pb–Br terminated CsPbBr$_3$ surface costs 0.23 eV less than in the bulk, demonstrating that this surface is prone to vacancy formation. However, if the surface is passivated with EDA-Br, the probability of creating Br vacancies is significantly reduced. Removing the original surface Br now even costs 0.19 eV more than a bulk Br and removing the newly added Br (together with EDA^{2+} ion) requires only 0.09 eV less than a bulk Br, see Figure 2c. These results indicate that addition of EDABr$_2$ efficiently passivates the 3D perovskite surface, suppressing the formation of halogen vacancies.

Calculations on the activation barriers of halogen vacancies suggest that halide migration is also suppressed. Specifically, while the diffusion of a Br vacancy between two layers separated
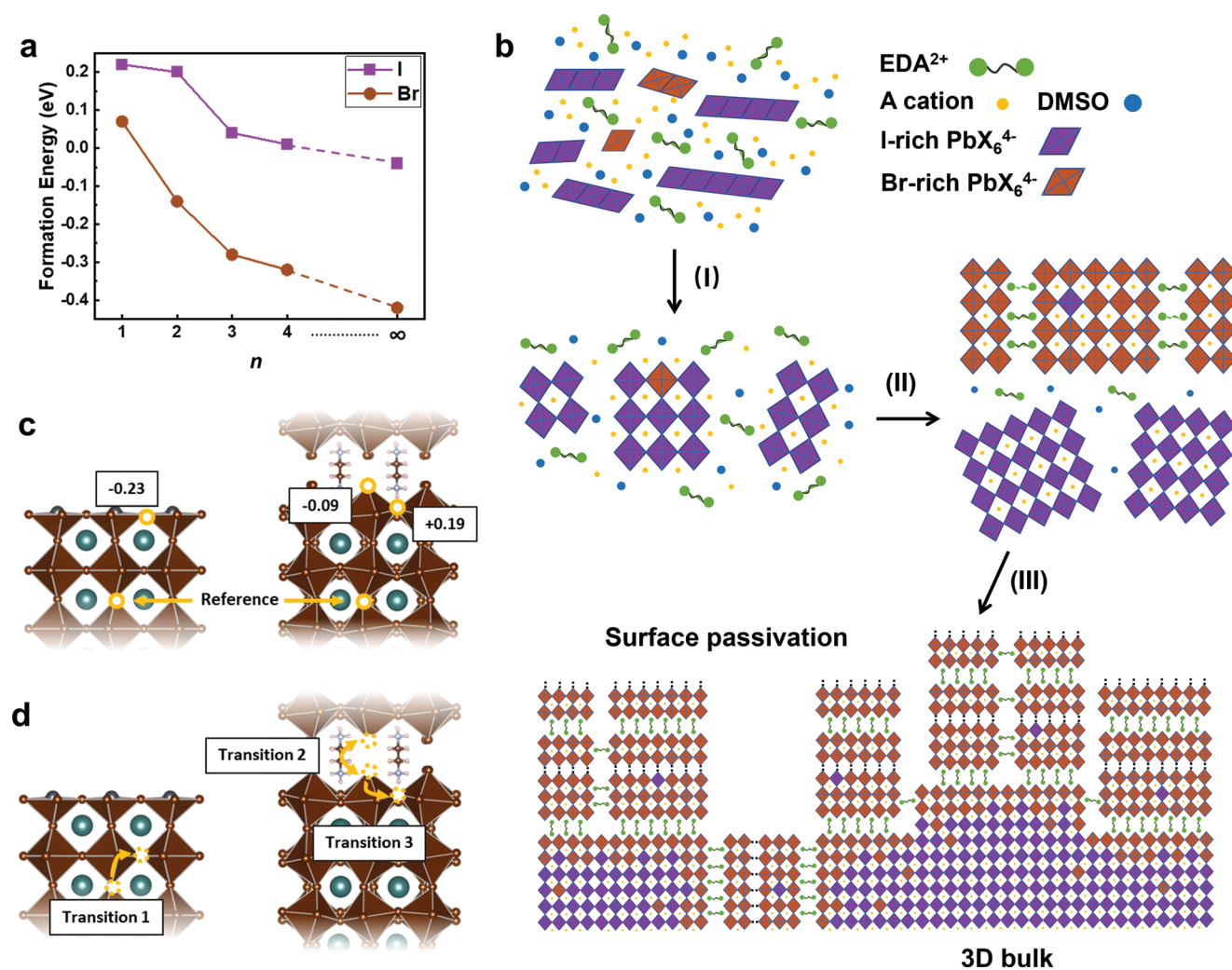
**ADVANCED
SCIENCE NEWS**

www.advancedsciencenews.com

**ADVANCED
MATERIALS**

www.advmat.de

Figure 2. Theoretical simulations on phase formation and vacancy formation. a) DFT calculated formation energies of $EDACs_{n-1}Pb_nX_{3n+1}$ (X = Br, I) perovskites for n = 1–4 and $n = \infty$ corresponding to 3D $CsPbX_3$ (X = Br, I). b) Schematic illustration of the crystallization process of the diammonium-modified film. Formation of the 3D perovskite grains (I) is followed by precipitation of a thin amorphous-like quasi-2D surface layer (II). c) Br vacancy formation energies on the $CsPbBr_3$ surface and at the $PbBr_6$-EDA interface, with respect to the bulk. d) Diffusion paths for Br vacancies in $CsPbBr_3$ (Transition 1) and $EDACs_3Pb_4Br_{13}$ (Transition 2 and 3). Transitions 1 and 3 are out-of-plane transitions in the bulk and EDA-saturated surface, respectively. Transition 2 is between two EDA^{2+} separated surfaces.

by EDA^{2+} (Figure 2d, Transition 2) has a barrier similar to that in the bulk (Figure 2d, Transition 1) (0.38 eV vs 0.37 eV), the out of plane diffusion at the EDA-Br passivated surface (Figure 2d, Transition 3) has a barrier of 0.50 eV, which is significantly higher than in the bulk (0.37 eV). This means that EDA^{2+} not only suppresses the formation of Br vacancies, but also increases the barriers for Br diffusion along the grain boundaries, therefore suppressing the migration of vacancy defects.

Passivating the 3D perovskite surface not only makes it more stable, but it also removes electronically harmful defects, as undercoordinated Pb ions can result in trap states for electrons inside the bandgap.[25] Such undercoordinated Pb sites are either already present at the $CsPbBr_3$ surface (Figure 2c), or they are created by Br vacancies. The passivation effect predicted by DFT was examined with optical and electronic measurements. First, we performed the time-resolved photoluminescence (TRPL) measurement (**Figure 3**a) under a low excitation fluence

of 5 nJ cm^{-2} at 485 nm. Under this low fluence the trap-assisted recombination process could significantly influence the PL decay curves.[26–28] The TRPL data was fitted with a biexponential function to mathematically extract the PL decay lifetime for comparison. The results show that both the fast-decay lifetime and slow-decay lifetime of the optimized perovskite films (with 20% $EDABr_2$) are extended, with the average lifetime drastically increasing from 206.24 to 909.02 ns (Table S2, Supporting Information). The result suggests reduced defects and improved radiative recombination by the addition of $EDABr_2$. Note that the decreased lifetime of the 60%-$EDABr_2$-treated film may be attributed to the poor crystallinity of the perovskite. We further fabricate electron-only and hole-only devices with structures of ITO/ZnO/PEIE/perovskite/TPBi/LiF/Al and ITO/PEDOT:PSS/perovskite/TFB/MoO$_3$/Au, respectively, to compare trap states in the control film and modified films. As shown in Figure 3b,c, three regions could be identified from
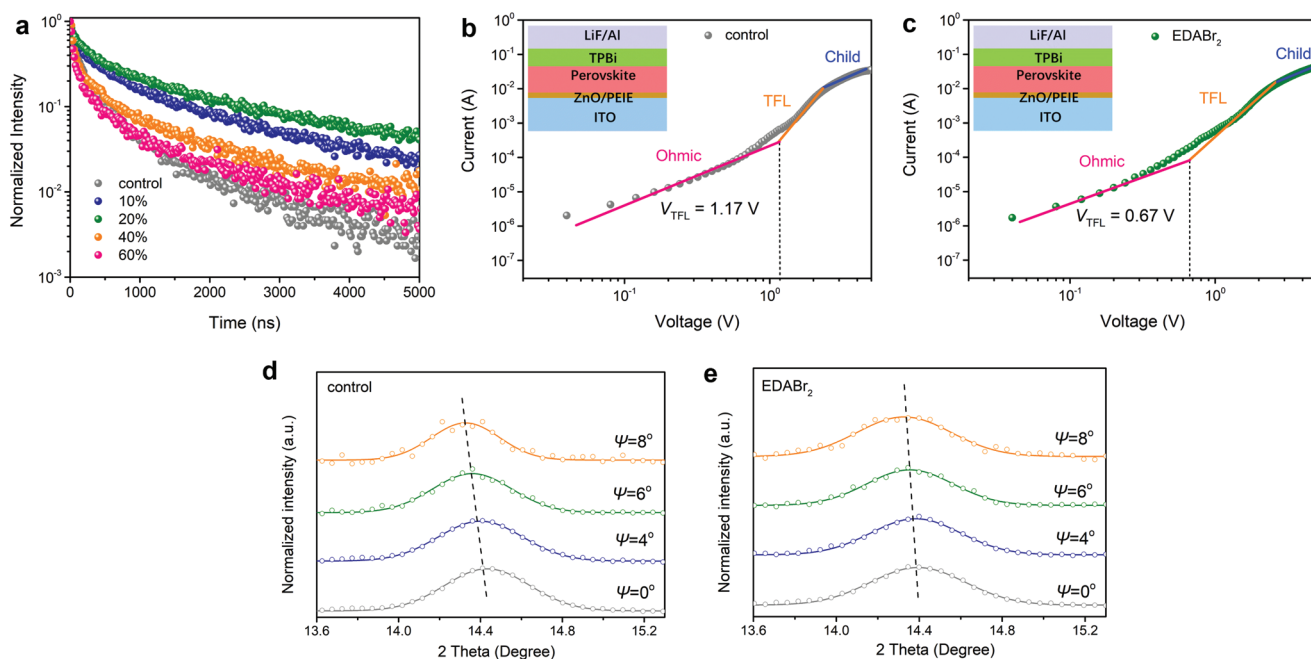
Figure 3. Characterizations of defects passivation in thin films. a) TRPL decay of the fabricated films. b,c) Current–voltage curves of electron-only devices based on the control (b) and modified perovskite (c). d,e) The inset figures illustrate the device structure. GIXRD of the control film (d) and modified film (e) with different instrumental ψ values.

the dark-current–voltage (I–V) curves, i.e., an ohmic region at low voltages (purple), a trap-filling limited (TFL) region at intermediate voltages (orange), and a trap-free Child's region at high voltages (blue).[29] In the TFL region of the I–V curve, the trap states are filled with the injected charges and the electron-only device exhibits a low-resistance state with rapidly increased current. The onset voltage of the TFL region, named as the trap-filled limited voltage (V_{TFL}), is proportional to the density of the trap states. Hence, the decreased V_{TFL} in the dark I–V curve of the electron-only device provides direct evidence of reduced electron traps in the modified film. In contrast, the hole-only device does not exhibit much improvement with EDABr$_2$ modification (Figure S8, Supporting Information). The observation of the reduced electron traps in the experiment is consistent with our DFT analysis, i.e., Br vacancies, which are known to introduce defect states near the conduction band and thus act as electron traps,[25] are reduced after the binding of EDA^{2+} to the Pb–Br framework.

Lastly, we carry out grazing-incidence X-ray diffraction (GIXRD) measurements to investigate the evolution of strain in the modified films. According to previous studies, a tensile strain in the film would manifest itself as a shift of the GIXRD peaks towards lower angles with the increasing instrument tilt angle ψ, and the greater the shift, the larger the strain.[30–34] By comparing Figure 3d,e, it is clear that the control film exhibits a significantly greater peak shift as compared to the EDABr$_2$-modified film, suggesting the tensile strain is reduced in the EDABr$_2$-modified film. This may suggest that EDA-Br phase can help reduce the perovskite lattice distortion possibly caused by the mismatch between the 3D perovskite and the ZnO layer underneath, and subsequently reduces defect formation in the perovskite films.[35]

We further examine the effect of the diammonium modification on the performance of red PeLEDs. The devices are fabricated with a typical architecture as shown in **Figure 4**a. Polyethyleneimine (PEIE)-modified zinc oxide (ZnO) and poly[(9,9-dioctylfluorenyl-2,7-diyl)-co-(4,4′-(N-(4-secbutylphenyl)diphenylamine)) (TFB) are employed as the electron injection layer and hole injection layer, respectively. The current density–voltage, luminance–voltage, EQE–current density, and current efficiency–voltage characteristics are compared and illustrated in Figure 4b,c and Figure S9 (Supporting Information). A higher EQE, luminance and current efficiency are obtained upon the addition of EDABr$_2$. The device with 20% EDABr$_2$ shows a peak EQE of 14.06% at 671.6 nm and a high luminance of 11 592 cd m^{-2} (Table S3, Supporting Information). According to the small down-shift of the band energy levels in the modified perovskite (by 0.04 and 0.05 eV for the conduction band and valence band, respectively) and the slight increase in electron injection and decrease in hole injection (Figures S8 and S12, Supporting Information), the charge injection is not significantly altered.

Finally, we introduce a passivator, commonly used in our previous work, 5-ammonium valeric acid iodide (5-AVAI), to further optimize the device.[11,36,37] The EDABr$_2$-modified device retains a high luminance of 10 745 cd m^{-2} and reaches a peak EQE of 17.03% at a high current density of 308 mA cm^{-2} with a current efficiency of 2.72 cd A^{-1} (**Figure 5**a,b and Figure S13, Supporting Information), while the control device exhibits a luminance of 4285 cd m^{-2}, a peak EQE of 8.35%, and a current efficiency of 1.09 cd A^{-1}. Notably, the superior EQE of over 17% in the optimized device is retained at a high current density of hundreds of milliamps per square centimeter, in stark contrast to the drastic efficiency drop of QLEDs at current density
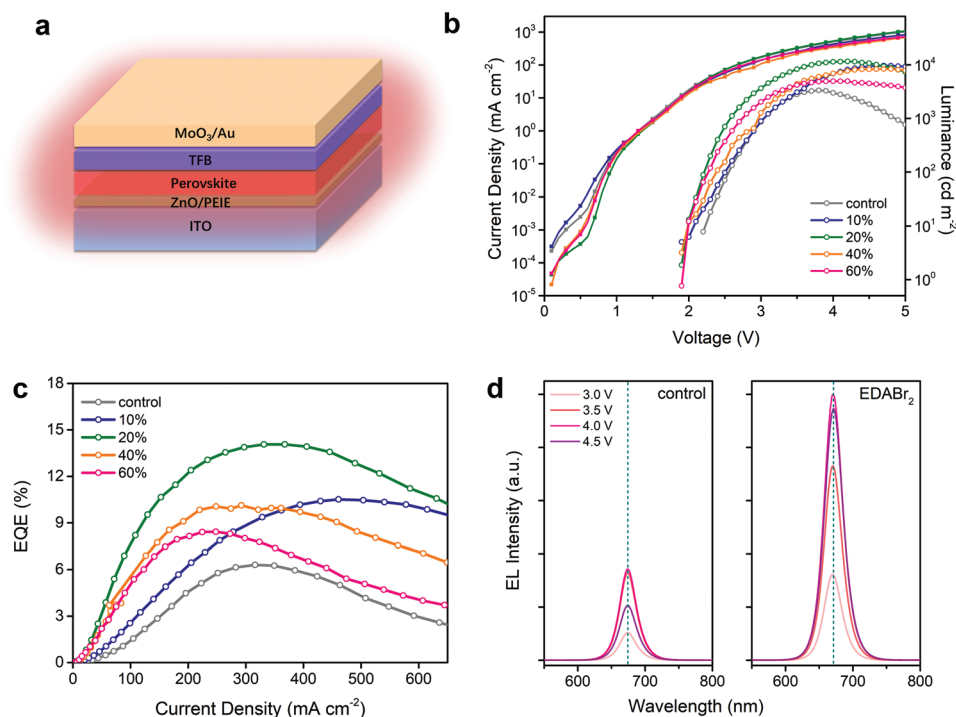
**ADVANCED
SCIENCE NEWS**

www.advancedsciencenews.com

**ADVANCED
MATERIALS**

www.advmat.de

Figure 4. Device characteristics of the fabricated PeLEDs. a) Schematic device architecture. b) Current density–voltage and luminance–voltage curves and c) EQE–current density curves of as-fabricated devices. d) EL spectra of the control and 20% $EDABr_2$-modified device.

higher than tens of milliamps per square centimeter.[4,5] The $EDABr_2$-modified devices exhibit a good reproducibility (Figure S14, Supporting Information) and the EL spectrum of the optimized device shows a narrow FWHM of 28 nm (Figure 5c) with Commission Internationale de l'Eclairage (CIE) coordinate (0.72, 0.28) (Figure S15, Supporting Information). Our optimized device sets a record for high-luminance and efficient red PeLEDs based on 3D perovskite films (Figure S16 and Table S4, Supporting Information). Moreover, we investigate the spectral stability of the fabricated device and no shift of the EL peak is observed with the increasing voltage (Figure S17, Supporting Information). The $EDABr_2$-modified device shows a half-lifetime (T_{50}) of 15.4 h (Figure 5d) compared to the device without $EDABr_2$ (T_{50} = 0.69 h), which is superior to most of the reported red PeLEDs. Our results demonstrate the great potential of mediating perovskite formation by diammonium molecules for fabricating bright, high-efficiency and stable red light-emitting devices.

3. Conclusions

This study has revealed the unique role of diammonium molecules in mediating the formation process of 3D mixed Br/I perovskite and demonstrated 3D perovskite-based red light-emitting devices with a record luminance and half-lifetime. The strong preferential interactions between the diammonium cations and the Pb-Br octahedra results in low formation energy of the corresponding quasi-2D phases, thus allowing for formation of an EDA-Br rich perovskite capping layer around the 3D perovskite grain surfaces. Such a structure appears to be

beneficial for defect reduction, suppression of ion migration, as well as decrease of lattice strain. As a result, both the efficiency and the operational stability at high current density of the $EDABr_2$ modified PeLEDs are substantially improved. Our findings highlight the potential of diammonium molecules in regulating film formation of mixed halide perovskites and could be applied to other perovskite systems for achieving efficient and stable perovskite optoelectronic devices.

4. Experimental Section

Materials: Cesium iodide (CsI, Sigma-Aldrich, 99.999%), lead iodide (PbI_2, TCI, 99.99%), lead thiocyanate (Pb(SCN)$_2$, Sigma-Aldrich, 99.5%), formamidinium bromide (FABr, Greatcell Solar Materials, 99.99%), ethylenediammonium dibromide ($EDABr_2$, Sigma-Aldrich, 98%), 5-ammonium valeric acid iodide (5-AVAI, Greatcell Solar Materials, 99%), polyethyleneimine (PEIE, 80% ethoxylated, 37% solution in H_2O, J&K), poly(9,9-dioctyl-fluorene-*co-N*-(4-butylphenyl)diphenylamine) (TFB, American Dye Source, Inc.), and molybdenum oxide (MoO_3, Sigma-Aldrich, 99.97%) were used as received. Colloidal zinc oxide (ZnO) nanocrystals were synthesized as reported in the literature.[38]

Preparation of Perovskite Precursors: The 0.13 M perovskite precursors were prepared by dissolving CsI, PbI_2, Pb(SCN)$_2$, FABr with a molar ratio of 1.7:0.5:0.5:1 in dimethyl sulfoxide (DMSO). For the diammonium-doped perovskite, 1 M diammonium solution in DMSO with a specified volume was added in the precursor.

Device Fabrication: The ITO glass substrates were washed by detergent, deionized water, acetone, ethanol, and isopropanol under ultrasonication, then dried by nitrogen flow and subsequently exposed to UV–ozone for 15 min before use. The synthesized ZnO nanoparticles were spin-coated on ITO substrates at 4000 rpm for 35 s, followed by annealing at 150 °C for 30 min. Then the PEIE solution (0.4 wt% in 2-methoxyethanol) was coated on top at 5000 rpm for 35 s and annealed
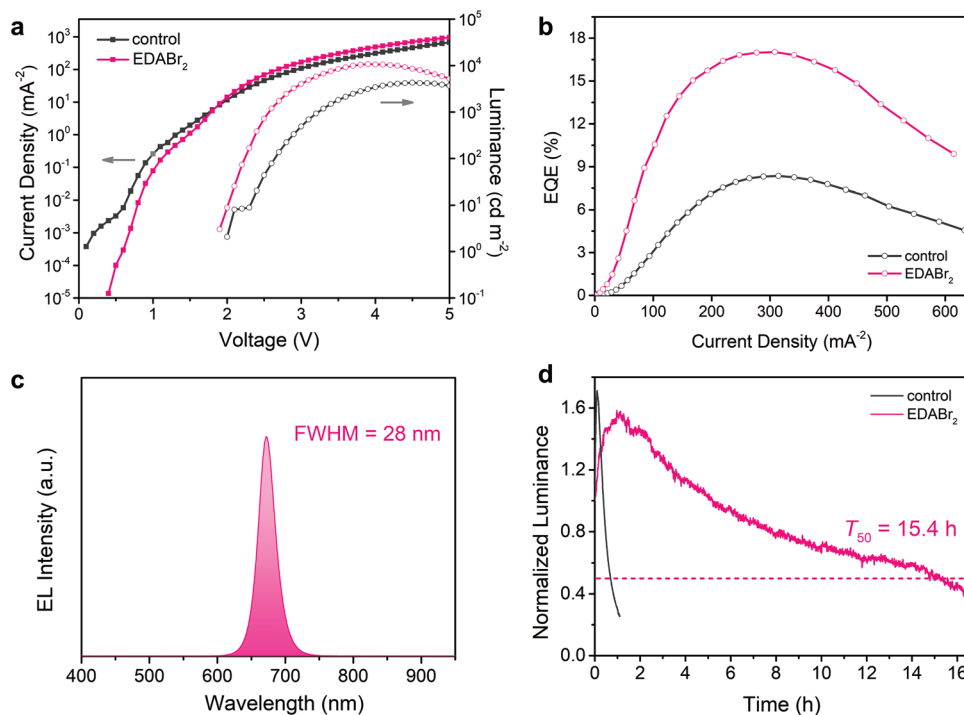
**ADVANCED
SCIENCE NEWS**

www.advancedsciencenews.com

**ADVANCED
MATERIALS**

www.advmat.de

Figure 5. Device performance and operation stability. a) Current density–voltage and luminance–voltage curves and b) EQE–current density curves of the fabricated devices. c) EL spectrum of the optimized EDABr$_2$-modified device at 4 V. d) Device operation stability under a constant current density of 20 mA cm^{-2}.

at 90 °C for 10 min. After cooling down, the substrates were transferred to the N$_2$ glovebox and washed by N,N-dimethylformamide (DMF) through a spin-coating process to leave an ultrathin PEIE. To prepare the perovskite films, the precursors were deposited on the PEIE-modified ZnO substrates by spin-coating at 8000 rpm for 20 s, and then annealed at 100 °C for 20 min. Subsequently, TFB (15 mg mL^{-1} in chlorobenzene) was deposited by spin-coating at 4000 rpm for 45 s. Finally, 7 nm MoO$_3$ and 50 nm Au were evaporated at 0.2 and 1 Å s^{-1} through a shadow mask under high vacuum.

Characterizations: The top-view SEM images were captured by a high-resolution field emission SEM (HR-FESEM, FEI, Quanta 400). The STEM samples were cut and thinned by FIB/SEM on Thermal Scios 2 and the cross-sectional HAADF-STEM images were collected by field-emission transmission electron microscopy (FEI TecnaiF20) at 200 kV. The XRD patterns were taken by an X-ray diffraction system with a Rigaku ru-300 diffractometer (Cu Kα irradiation, λ = 1.5406 Å). The absorption spectra were recorded by a Hitachi U-3501 UV–Vis–NIR spectrophotometer. The steady-state PL was measured by a continuous-wave laser source with a wavelength of 405 nm. The TRPL decay was carried out by an FLS980 spectrofluorometer (Edinburgh Instruments), excited by a 485 nm laser with a low fluence of 5 nJ cm^{-2}. Transient absorption measurements were performed using a Ti:sapphire regenerative amplifier laser (Coherent Legend Elite) system, producing a 100 fs pulses at 3.5 mJ at 800 nm at 1 kHz repetition rate. The amplifier beam was split into two. One beam pumps an optical parametric amplifier (Coherent OPerA Solo) generating 285 nm pump pulses that is chopped at 500 Hz, and then directed onto the sample. Another beam from the amplifier was diverted onto a mechanical delay stage and then focused onto a 2 mm CaF$_2$ plate which generated a broadband supercontinuum acting as the probe beam. The probe beam was focused onto the sample surface with an achromatic lens, spatially overlapping with the pump beam. The transmission of the probe was measured by a spectrometer (Acton Spectrapro 275) equipped with a grating (50 lines per mm) and a CCD line array synchronized with the probe laser repetition rate. The transmission spectrum was recorded continuously (1 kHz) and the

differential signal was taken at each time delay point by $(T_{on} - T_{off})/T_{off}$. XPS measurement was performed in a VG ESCALAB 220i-XL surface analysis system equipped with a monochromatic Al KαX-ray gun (hν = 1486.6 eV). The device performance was tested with a Keithley 2400 source meter and a QE-Pro spectrometer coupled with a fiber integration sphere (FOIS-1).

First Principles Calculations: DFT calculations were performed using the Projector Augmented Wave (PAW) method as implemented in the Vienna Ab initio Simulation Package (VASP). The electronic exchange–correlation interaction was described by the functional of Perdew, Burke, and Ernzerhof (PBE) within the generalized gradient approximation (GGA). Energy and force convergence criteria of 10^{-5} eV and 10^{-2} eV Å^{-1}, respectively, were used in all calculations. The D3 correction with Becke–Jonson damping was employed to account for the van der Waals interactions due to the presence of the organic cations.

For the 3D perovskite formation energy calculations tetragonal CsPbX$_3$ (X = Br, I) unit cells of 20 atoms were used, along with a 12 × 12 × 4 Monkhorst–Pack k-point grid. The 2D perovskites structural models were 2 × 2 × 1 supercells of 76, 96, 116, and 136 atoms for n = 1, 2, 3, and 4 respectively and for the corresponding calculations a 3 × 3 × 2 Monkhorst–Pack k-point grid was employed. In all cases the kinetic energy cutoff was set to 500 eV. The perovskite formation energies were given as

$$E_{form,2D} = E_{EDACs_{n-1}Pb_nX_{3n+1}} - nE_{PbX_2} - (n-1)E_{CsX} - E_{EDAX_2} \qquad (1)$$

$$E_{form,3D} = E_{CsPbX_3} - E_{PbX_2} - E_{CsX} \qquad (2)$$

For the defect calculations a 4-layer slab of 2×2 CsPbBr$_3$ with a vacuum region of ≈20 Å separating the slabs was used and a 4×4×1 k-point grid. The same structure as before was employed for EDACs$_3$Pb$_4$Br$_{13}$. The diffusion barriers were calculated using the climbing image nudged elastic band (CINEB) method, with a force criterion of 5 × 10^{-2} eV Å^{-1} and five intermediate geometries for the transition state search.

**ADVANCED
SCIENCE NEWS**

www.advancedsciencenews.com

**ADVANCED
MATERIALS**

www.advmat.de

Supporting Information

Acknowledgements

Conflict of Interest

The authors declare no conflict of interest.

Data Availability Statement

The data that support the findings of this study are available from the corresponding author upon reasonable request.

Keywords

[1] Z.-K. Tan, R. S. Moghaddam, M. L. Lai, P. Docampo, R. Higler, F. Deschler, M. Price, A. Sadhanala, L. M. Pazos, D. Credgington, F. Hanusch, T. Bein, H. J. Snaith, R. H. Friend, *Nat. Nanotechnol.* **2014**, *9*, 687.

[2] J. H. Heo, J. K. Park, S. H. Im, *Cell Reports Phys. Sci.* **2020**, *1*, 100177.

[3] Y.-K. Wang, F. Yuan, Y. Dong, J.-Y. Li, A. Johnston, B. Chen, M. I. Saidaminov, C. Zhou, X. Zheng, Y. Hou, K. Bertens, H. Ebe, D. Ma, Z. Deng, S. Yuan, R. Chen, L. K. Sagar, J. Liu, J. Fan, P. Li, X. Li, Y. Gao, M.-K. Fung, Z.-H. Lu, O. M. Bakr, L.-S. Liao, E. H. Sargent, *Angew. Chem., Int. Ed.* **2021**, *60*, 16164.

[4] T. Chiba, Y. Hayashi, H. Ebe, K. Hoshi, J. Sato, S. Sato, Y.-J. Pu, S. Ohisa, J. Kido, *Nat. Photonics* **2018**, *12*, 681.

[5] Y. Hassan, J. H. Park, M. L. Crawford, A. Sadhanala, J. Lee, J. C. Sadighian, E. Mosconi, R. Shivanna, E. Radicchi, M. Jeong, C. Yang, H. Choi, S. H. Park, M. H. Song, F. De Angelis, C. Y. Wong, R. H. Friend, B. R. Lee, H. J. Snaith, *Nature* **2021**, *591*, 72.

[6] J. Qing, S. Ramesh, Q. Xu, X.-K. Liu, H. Wang, Z. Yuan, Z. Chen, L. Hou, T. C. Sum, F. Gao, *Adv. Mater.* **2021**, *33*, 2104381.

[7] Y. Tian, C. Zhou, M. Worku, X. Wang, Y. Ling, H. Gao, Y. Zhou, Y. Miao, J. Guan, B. Ma, *Adv. Mater.* **2018**, *30*, 1870142.

[8] L. Zhang, C. Sun, *Light Sci. Appl.* **2021**, *10*, 61.

[9] Y. Jiang, J. Wei, M. Yuan, *J. Phys. Chem. Lett.* **2021**, *12*, 2593.

[10] C. Yi, C. Liu, K. Wen, X.-K. Liu, H. Zhang, Y. Yu, N. Fan, F. Ji, C. Kuang, B. Ma, C. Tu, Y. Zhang, C. Xue, R. Li, F. Gao, W. Huang, J. Wang, *Nat. Commun.* **2020**, *11*, 4736.

[11] Z. Fang, W. Chen, Y. Shi, J. Zhao, S. Chu, J. Zhang, Z. Xiao, *Adv. Funct. Mater.* **2020**, *30*, 1909754.

[12] Y. Ke, N. Wang, D. Kong, Y. Cao, Y. He, L. Zhu, Y. Wang, C. Xue, Q. Peng, F. Gao, W. Huang, J. Wang, *J. Phys. Chem. Lett.* **2019**, *10*, 380.

[13] B. Han, B. Cai, Q. Shan, J. Song, J. Li, F. Zhang, J. Chen, T. Fang, Q. Ji, X. Xu, H. Zeng, *Adv. Funct. Mater.* **2018**, *28*, 1804285.

[14] J. Ye, M. M. Byranvand, C. O. Martínez, R. L. Z. Hoye, M. Saliba, L. Polavarapu, *Angew. Chem., Int. Ed.* **2021**, *60*, 21636.

[15] G. Sun, X. Liu, Z. Liu, D. Liu, F. Meng, Z. Li, L. Chu, W. Qiu, X. Peng, W. Xie, C. Shen, J. Chen, H.-L. Yip, S.-J. Su, *Adv. Funct. Mater.* **2021**, *31*, 2106691.

[16] G. Cheng, Y. Liu, T. Chen, W. Chen, Z. Fang, J. Zhang, L. Ding, X. Li, T. Shi, Z. Xiao, *ACS Appl. Mater. Interfaces* **2020**, *12*, 18084.

[17] J. Gong, M. Hao, Y. Zhang, M. Liu, Y. Zhou, *Angew. Chem., Int. Ed.* **2022**, e202112022.

[18] S. Yuequn, L. Yuan, W. Qi, W. Ziyu, X. Bo, K. Youqi, L. Weimin, N. Zhijun, *Sci. Adv.* **2021**, *5*, eaaw8072.

[19] S. Yuan, Z.-K. Wang, L.-X. Xiao, C.-F. Zhang, S.-Y. Yang, B.-B. Chen, H.-T. Ge, Q.-S. Tian, Y. Jin, L.-S. Liao, *Adv. Mater.* **2019**, *31*, 1904319.

[20] K. H. Ngai, Q. Wei, Z. Chen, X. Guo, M. Qin, F. Xie, C. C. S. Chan, G. Xing, X. Lu, J. Chen, K. S. Wong, J. Xu, M. Long, *Adv. Opt. Mater.* **2021**, *9*, 2100243.

[21] H. Cho, S.-H. Jeong, M.-H. Park, Y.-H. Kim, C. Wolf, C.-L. Lee, J. H. Heo, A. Sadhanala, N. Myoung, S. Yoo, S. H. Im, R. H. Friend, T.-W. Lee, *Science* **2015**, *350*, 1222.

[22] Z. Xiao, R. A. Kerner, L. Zhao, N. L. Tran, K. M. Lee, T.-W. Koh, G. D. Scholes, B. P. Rand, *Nat. Photonics* **2017**, *11*, 108.

[23] Y. Cao, N. Wang, H. Tian, J. Guo, Y. Wei, H. Chen, Y. Miao, W. Zou, K. Pan, Y. He, H. Cao, Y. Ke, M. Xu, Y. Wang, M. Yang, K. Du, Z. Fu, D. Kong, D. Dai, Y. Jin, G. Li, H. Li, Q. Peng, J. Wang, W. Huang, *Nature* **2018**, *562*, 249.

[24] H. Wang, X. Zhang, Q. Wu, F. Cao, D. Yang, Y. Shang, Z. Ning, W. Zhang, W. Zheng, Y. Yan, S. V. Kershaw, L. Zhang, A. L. Rogach, X. Yang, *Nat. Commun.* **2019**, *10*, 665.

[25] H. Xue, G. Brocks, S. Tao, *arXiv* 2112.15251, **2021**.

[26] C. Wehrenfennig, G. E. Eperon, M. B. Johnston, H. J. Snaith, L. M. Herz, *Adv. Mater.* **2014**, *26*, 1584.

[27] D. W. deQuilettes, S. M. Vorpahl, S. D. Stranks, H. Nagaoka, G. E. Eperon, M. E. Ziffer, H. J. Snaith, D. S. Ginger, *Science* **2015**, *348*, 683.

[28] Y. Miao, Y. Ke, N. Wang, W. Zou, M. Xu, Y. Cao, Y. Sun, R. Yang, Y. Wang, Y. Tong, W. Xu, L. Zhang, R. Li, J. Li, H. He, Y. Jin, F. Gao, W. Huang, J. Wang, *Nat. Commun.* **2019**, *10*, 3624.

[29] D. Shi, V. Adinolfi, R. Comin, M. Yuan, E. Alarousu, A. Buin, Y. Chen, S. Hoogland, A. Rothenberger, K. Katsiev, Y. Losovyj, X. Zhang, P. P. Dowben, O. F. Mohammed, E. H. Sargent, O. M. Bakr, *Science* **2015**, *347*, 519.

[30] N. Yang, C. Zhu, Y. Chen, H. Zai, C. Wang, X. Wang, H. Wang, S. Ma, Z. Gao, X. Wang, J. Hong, Y. Bai, H. Zhou, B.-B. Cui, Q. Chen, *Energy Environ. Sci.* **2020**, *13*, 4344.

[31] C. Zhu, X. Niu, Y. Fu, N. Li, C. Hu, Y. Chen, X. He, G. Na, P. Liu, H. Zai, Y. Ge, Y. Lu, X. Ke, Y. Bai, S. Yang, P. Chen, Y. Li, M. Sui, L. Zhang, H. Zhou, Q. Chen, *Nat. Commun.* **2019**, *10*, 815.

[32] H. Zhang, Z. Chen, M. Qin, Z. Ren, K. Liu, J. Huang, D. Shen, Z. Wu, Y. Zhang, J. Hao, C. Lee, X. Lu, Z. Zheng, W. Yu, G. Li, *Adv. Mater.* **2021**, *33*, 2008487.

[33] Z. Liu, W. Qiu, X. Peng, G. Sun, X. Liu, D. Liu, Z. Li, F. He, C. Shen, Q. Gu, F. Ma, H.-L. Yip, L. Hou, Z. Qi, S.-J. Su, *Adv. Mater.* **2021**, *33*, 2103268.

[34] D.-J. Xue, Y. Hou, S.-C. Liu, M. Wei, B. Chen, Z. Huang, Z. Li, B. Sun, A. H. Proppe, Y. Dong, M. I. Saidaminov, S. O. Kelley, J.-S. Hu, E. H. Sargent, *Nat. Commun.* **2020**, *11*, 1514.

[35] D. Liu, D. Luo, A. N. Iqbal, K. W. P. Orr, T. A. S. Doherty, Z.-H. Lu, S. D. Stranks, W. Zhang, *Nat. Mater.* **2021**, *20*, 1337.

[36] Y. Guo, S. Apergi, N. Li, M. Chen, C. Yin, Z. Yuan, F. Gao, F. Xie, G. Brocks, S. Tao, N. Zhao, *Nat. Commun.* **2021**, *12*, 644.

[37] Y.-H. Jia, S. Neutzner, Y. Zhou, M. Yang, J. M. F. Tapia, N. Li, H. Yu, J. Cao, J.-P. Wang, A. Petrozza, C.-P. Wong, N. Zhao, *Adv. Funct. Mater.* **2020**, *30*, 1906875.

[38] J. Wang, N. Wang, Y. Jin, J. Si, Z.-K. Tan, H. Du, L. Cheng, X. Dai, S. Bai, H. He, Z. Ye, M. L. Lai, R. H. Friend, W. Huang, *Adv. Mater.* **2015**, *27*, 2311.